Evolution of prototyping in automotive engineering: a comprehensive study on the reliability of Additive Manufacturing for advanced powertrain components

Silvia Cecchel*, Riccardo Ferraresi, Matteo Magni, Leonardi Guerini
Streparava SpA, Via Zocco 13, 25030 Adro (BS), Italy
s.cecchel@streparava.com, https://orcid.org/0000-0002-2268-9596
r.ferraresi@streparava.com, m.magni@streparava.com, l.guerini@streparava.com

Giovanna Cornacchia
Department of Mechanical and Industrial Engineering, University of Brescia, via Branze 38, 25123 Brescia, Italy
giovanna.cornacchia@unibs.it, https://orcid.org/0000-0001-7953-0319

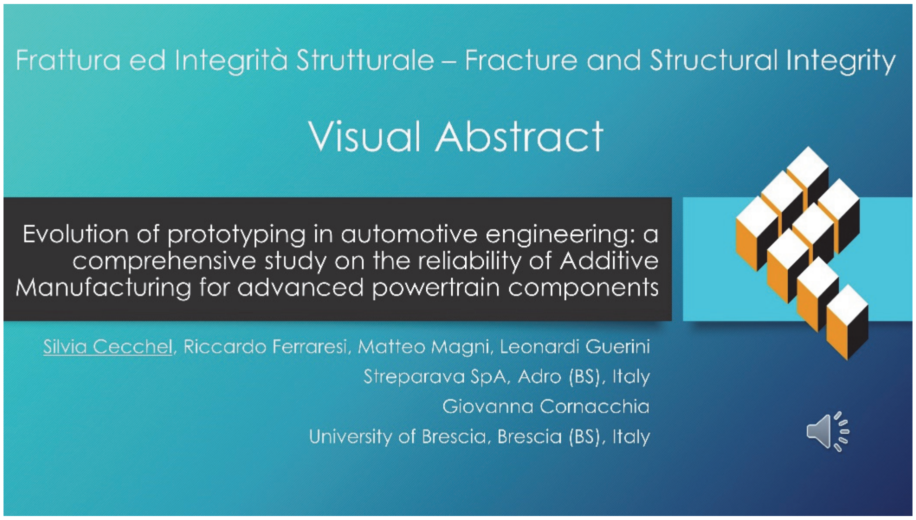
Frattura ed Integrità Strutturale – Fracture and Structural Integrity

Visual Abstract

Evolution of prototyping in automotive engineering: a comprehensive study on the reliability of Additive Manufacturing for advanced powertrain components

Silvia Cecchel, Riccardo Ferraresi, Matteo Magni, Leonardi Guerini
Streparava SpA, Adro (BS), Italy
Giovanna Cornacchia
University of Brescia, Brescia (BS), Italy

Citation: Cecchel, S., Ferraresi, R., Magni, M., Guerini, L., Cornacchia, G., Evolution of prototyping in automotive engineering: a Comprehensive Study on the reliability of Additive Manufacturing for advanced powertrain components, Frattura ed Integrità Strutturale, 68 (2024) 109-126.

Received: 04.12.2023
Accepted: 11.01.2024
Published: 22.01.2024
Issue: 01.04.2024

Copyright: © 2024 This is an open access article under the terms of the CC-BY 4.0, which permits unrestricted use, distribution, and reproduction in any medium, provided the original author and source are credited.

KEYWORDS. Engine test bench, Microstructure, Shape factor, Mechanical properties, Additive manufacturing, Automotive.

INTRODUCTION

The increasing importance of emission reduction in the automotive industry has led to the engineering of new parts and systems. Effective solutions can be innovations in the field of energy-efficient engines. In this context, the development of new products is a very relevant phase but, on the other hand, it can be costly and time-consuming.

Recently, researchers have attempted to adopt Additive Manufacturing (AM) to make small serial quantities of structural and functional parts, such as engine exhausts, drive shafts, gearbox components, braking systems [1], and conrods [2,3,4] for luxury, low-volume vehicles, and motorsports, where lightweight and highly complex structures can lead to relevant advantages. This is an innovative approach mainly because automotive serial production volumes are very high (greater than 100'000 parts per year) and currently not feasible through AM [5]. Thus, in the automotive field, AM is mostly used to obtain cost-effective prototypes within a short time [1]. Prototypes play an important role in the development of new structural products. They are subjected to functional tests and serve as demonstrators to determine whether a product is ready to move to the production stage [6]. Thus, the design, material, and technology of prototypes are relevant items that must be as representative as possible for the final manufacture. One disadvantage of AM is that the raw materials currently comprise a low range of alloys that can be employed. The most appropriate alloy must be selected based on its best match with serial applications in terms of chemical composition, microstructure, and mechanical properties. The post-processing plays a fundamental role in improving the quality of the parts, ensuring that they meet their design specifications. The AM process generates highly localized and high heat inputs in short interaction times, causing residual stress development, which affects the microstructure and mechanical behavior. Therefore, specific heat treatments must be developed for these alloys to produce the final preferred microstructures of AM products [2]. On the other hand, it would be of great interest to investigate the opportunity to adopt the most proper available AM for the prototypes production in order to guarantee a very short time to market, always needed it this phase of the project. The alloys available for AM prototypes could be different from that of the serial production, due to the reasons explained before, and the applicability of a change of material as to be properly evaluated.

The objective of this study is to evaluate the reliability of AM applications for the structural prototyping of a new powertrain system, a rocker arm, finalized to reduce vehicle emissions. A rocker arm is a valve-train component in internal combustion engines that controls the opening and closing of the engine valves. When the rocker arm is activated by a camshaft lobe, it transmits the camshaft movement toward the intake and exhaust valves of the engine. Therefore, fuel and air can be drawn into the combustion chamber during the intake stroke and exhaust gases can be expelled during the exhaust stroke. In recent years, improvements in rocker arm functions have been made, particularly with respect to increases in combustion and volumetric efficiencies, and construction materials [7]. In particular, the innovative product developed during this project is a switchable rocker arm [8] that can control the lift of a valve bridge, a single valve, or a valve train group of an internal combustion engine. The switchable rocker arm under investigation is shown in Fig. 1. It comprises a cam body (named 1), which is configured to be rotated by a cam, and a valve body (named 2), which is configured to act upon the valve bridge or a single valve (3). Valve springs (4), adjustment screws (5), and camshafts (6) were also identified. This particular rocker arm can be selectively switched between the first configuration, in which the rotation of the cam body around the axis generates a movement of the valve body, and the second configuration, in which the rotation of the cam body around the axis does not generate any movement of the valve body. Thus, when the system is enabled, one or more engine pistons will be disabled if they are not required for operation. In the cylinder deactivation mode, engine pumping losses are minimized, and the engine runs more efficiently. In this way, it is possible to reduce fuel consumption and therefore CO2 emissions, toward a more efficient and low-emissions engine, exactly the aim of this innovation.

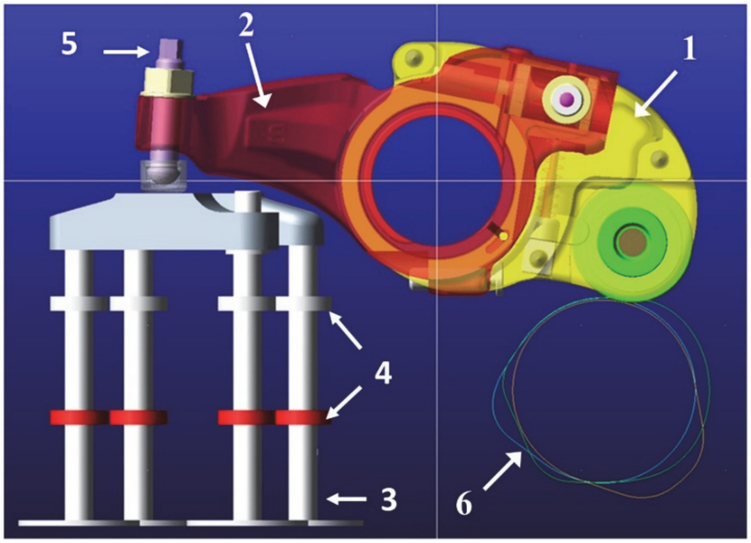

Figure 1: Switchable rocker configuration.

This is a critical assembly in a vehicle engine with a relevant structural function, and the volumes of production are high; thus, serial production is designed using forged steel (42CrMo4+QT). As already mentioned, the materials that can be currently employed with AM processes are limited and 42CrMo4 is not commercially diffused at this time. Thus, the closest alloy widely diffused for the production of AM prototypes was 17-4PH alloy, that has to be heat treated in the proper way. In particular, the target desired was to achieve mechanical properties similar to that of the forged serial production. 17-4PH is a martensitic stainless steel strengthened by precipitation of Cu-rich spherical particles showing a good combination of high tensile strength, toughness, and corrosion resistance [9-11]. From a microstructural point of view, laser powder bed fusion (LPBF) as-built (AB) samples present a dendritically solidified microstructure consisting of martensite with high amounts of residual austenite, in contrast to wrought samples that present a fully martensitic microstructure [12]. This microstructural difference is due to the formation of small grains originating from rapid solidification undercooling and the presence of retained nitrogen from N2-atomization that may suppress the formation of martensite at room temperature in the as-built material, leading to a metastable austenitic microstructure [12, 13]. Note that the retained austenite negatively affects the strength of the alloy, improves the ductility [14] and strongly reduces the strengthening effect of the aged heat treatment [13].

In the literature, many studies have been conducted on the effects of heat treatment on mechanical properties and microstructural features [11,15-23]. The rapid solidification typical of AM can lead to ultrafine microstructures, which could be suitable for structural applications without the need for further heat treatment [24]. The AM as-built condition usually has a more heterogeneous microstructure than conventional manufacturing, and in general, heat treatments are required to produce a final preferred microstructure and optimize the mechanical properties. Among the different heat treatments available for this alloy, a typical method involves solution annealing at approximately 1050–1150°C for 1 h [11,15,16,18,21] to dissolve the alloying elements in the austenitic matrix, followed by quenching, which results in the formation of martensite. This treatment also helps the removal of patterns and the laser scan footprint by homogenizing the microstructure [15,16]. For example, Cheruvathur et al. [15] found that solution heat treatment (1050°C, 1h) was an effective way to lower the volume fraction of austenite, while higher-temperature solution heat treatment (1150°C, 2h) was more incisive to alleviate microsegregation.

The thickness of additively manufactured components is an important aspect to be considered. In fact, the higher the thickness, the higher the number of layers welded, which could affect the heat dissipation and/or number of defects. Thus, the evaluation of the potential effects of geometries on manufacturing properties is an important topic to be investigated, particularly from the perspective of real component production. In the literature, few studies have been conducted on the effect of AM sample thickness [25-33] and, to the best of the authors' knowledge, none of them is about 17-4PH steel. Regarding steel alloys, the studies analyzed agreed in finding a decrease in mechanical properties when the thicknesses are reduced [29-33]. Roughness appears to be the main explanation for this phenomenon, and Leicht et al. [29] identified the influence of roughness on the elongation percentage of 316 L SLM samples. Indeed, when the thickness is reduced, the surface area/volume ratio increases and the effect of surface irregularities becomes more relevant. Brown et al. [29] studied 304 L SLMed samples and agreed that the surface roughness effect on both the strength and elongation decreased with thickness. Roach et al. [31] confirmed the same trend on 316 L samples, observed both strength and Young 's modulus, and explained that the surface roughness acts via two mechanisms: decreasing the effective load-bearing area and creating stress concentration. Koyama et al. [32] showed that below a critical thickness of 316 L sheet, the strength decrease was caused by the relationship between the thickness and average grain size. Chan and Fu [33] clarified that when the wall thickness decreases, the load is reduced by fewer grains, and inhomogeneous deformation is present. Finally, Leicht et al. [29] attributed the lower strength observed for the thinnest samples to the intensification of the defect effect owing to the surface-to-volume ratio of the specimen.

For all the purposes explained above, the present study investigates the mechanical behavior, microstructure features, and effects of the sample geometry and size, as well as the effects of heat treatments, on samples made of AM 17-4PH steel. First, samples with different volumes and shapes were produced. Subsequently, microstructural and mechanical characterizations were performed to verify the properties obtained under the different thermal treatment conditions. Understanding these characteristics is fundamental for properly designing rocker arm prototypes that are then produced using the same alloy and technology. FEA was also performed to assess the structural resistance of the new product under representative lifetime conditions. Finally, the prototypes were produced, analyzed, and verified on a test bench to evaluate their reliability during demanding applications. The conclusions of this project have laid the basis for similar future applications of time-effective prototypes, which can be dimensioned owing to appositely developed post-processes that guarantee the required resistance, even with a small range of currently available AM alloys.

MATERIALS AND METHODS

Materials description

The switchable rocker arm system is described in the introduction section. In particular, the cam body was the sub-component studied in this work and was prototyped using the LPBF process. The cam body in serial production was made of the 42CrMo4 EN 10083-3 alloy. One of the most common steels manufactured through LPBF is the 17-4 PH steel alloy, which can achieve mechanical properties similar to those of 42CrMo4 after heat treatment; thus 17-4 PH powder was selected for the prototype. To check the properties and determine the best configuration for the application, samples with various thicknesses were manufactured and tested under both as-built and heat-treated conditions. The experimental characterization performed to evaluate the performance is presented in the following sections.

The tensile test samples and engine components (rocker arm) used for the characterization in this study were produced by using a Laser powder bed fusion (LPBF) M2 Laser series 5 (Concept Laser GmbH, Germany) machine under an argon atmosphere. The building platform has dimensions of 245 x 245 mm^2, a dual-laser system and a layer thickness of 25 μm were used. The powder average diameter was 40 μm and its chemical compositions is listed in Tab. 1.

Elements	Cr	Ni	Cu	Si	Mn	Nb	C	V
%wt	16.2	4.02	3.72	0.78	0.33	0.29	0.036	0.018
Co	P	W	S	Sn	Mo	Ti	Al	Fe
0.012	0.009	0.009	0.004	0.004	0.002	0.002	0.001	Balance

Table 1: Chemical composition of 17-4PH steel powder.

The samples were built with the main length along the building direction. Both flat and cylindrical tensile test specimens were analyzed to evaluate the potential effects of geometry and thickness. The dimensions are shown in Fig. 2.

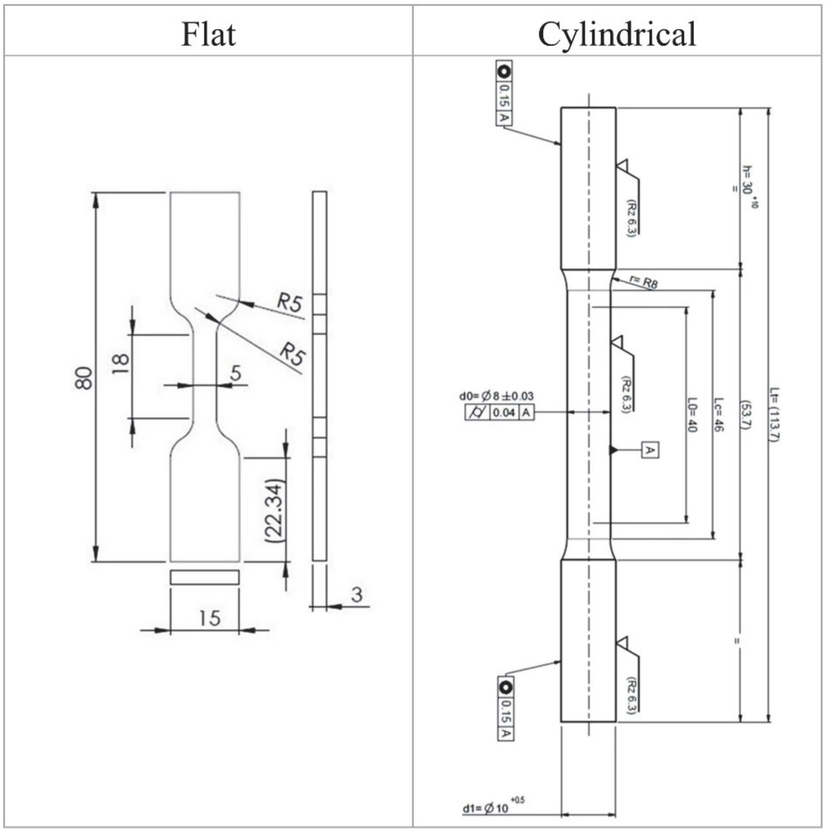

Figure 2: Tensile test specimens, flat sample on the left and cylindrical sample on the right.

All the samples were tested in the unmachined condition to be as reliable as possible from the perspective of an AM application, where most of the component surfaces are usually not machined. Both batches were analyzed under two different conditions: as-built (AB) and solution heat treatment (S). This thermal treatment consisted of the first step of heating at 990°C for 40 min, followed by a second step at 1040°C for 50 min, followed by an argon quenching in furnace (cooling rate ~32 °C/min). In addition, some prototypes of the cam body rocker arm (Fig. 3) were realized using LPBF under the same conditions as the described samples. In particular, two symmetrical parts of the prototypes showed in Fig. 3 are assembled together in the final system in order to compose the entire cam body (see element 1 of Fig. 1).
The influence of both the heat-treatment conditions and volume of the samples was investigated through microstructural analyses. The mechanical properties of 42CrMo4+QT considered as reference are: σ_m=925 MPa; $\sigma_{p0.2}$=740 MPa; A=15% [34].

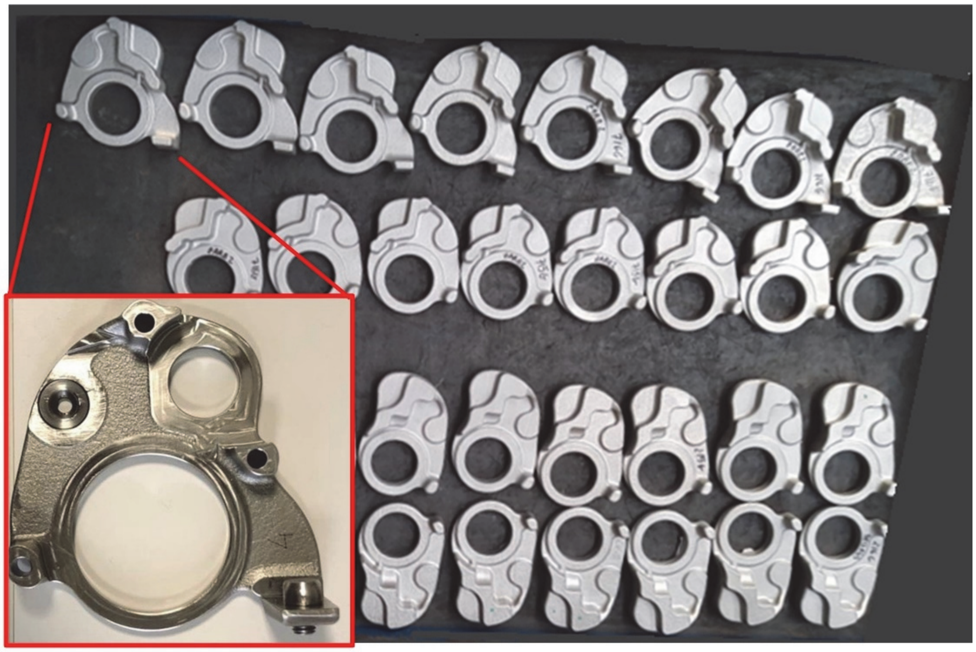

Figure 3: 17-4 PH cam body prototypes realized with the LPBF technique.

Microstructural observation and analysis

Microstructural analysis was performed on the samples cut off from the shoulders of the tensile test specimens and from several areas of the body. Both the longitudinal and transverse sections were analyzed. All the studied surfaces were prepared using standard metallographic techniques, that is, ground with SiC papers and polished with 1µm diamond paste. Chemical etching was performed by immersion in Kalling's reagent (5 g $CuCl_2$, 100 ml HCl, and 100 ml ethanol) for approximately 30 s at room temperature. The highlighted microstructure was observed using a Leica DMI 5000M optical microscope (OM), a LEO EVO 40 Scanning Electron Microscope (SEM). Semi-quantitative chemical analyses were obtained by means of an EDS (Energy Dispersive Spectroscopy–Link Analytical eXL) probe, with a spatial resolution of a few microns. Elemental mapping analyses were carried out. Panalytical X'Pert PRO diffractometer equipped with a X'Celerator detector was used for X-ray diffraction (XRD). X-ray source was Cu Kα ,λ = 0.154nm and the generator Settings were 40 mA, 40 kV. XRD patterns were collected at room temperature in a 2θ range of 35° ÷ 105° (Step Size: 0.008° 2θ; Scan Step Time: 40 s). Spectra analyses were performed by using X'Pert Highscore Plus software.

Hardness and tensile test

Vickers microhardness (HV) profiles were obtained for the transverse and longitudinal sections, both on flat cylindrical specimens and engine components. HV tests were performed with a Micro Duromat 4000 Reichert Jung instrument, according to ASTM E92-16, using a 500 g load applied for 10 s on the polished surface.
Tensile tests were performed to evaluate Young's modulus (E), yield strength ($\sigma_{p0.2}$), ultimate tensile strength (σ_m), and elongation at failure (A%) under each examined condition. For the flat specimens, an electromechanical testing machine (Instron 3369) equipped with a 50 kN load cell was used, whereas for the cylindrical specimens, a load-controlled servo-hydraulic testing machine (Instron 8501) with a 100 kN load cell was employed. In both cases, strain measurement was

carried out using an extensometer with a strain rate of 1 mm/min at room temperature (approximately 25°C and 30% relative humidity), following UNI EN ISO 6892-1:2020. Three samples were tested for each condition.

Multibody analysis and Finite element Analysis

Test benches are usually a fundamental step of the product validation. It is relevant to remember that the current characterization belongs to a wider innovation project, the development of a switchable rocker arm. In this specific case, the test bench was a functional engine test finalized at evaluating the operation of the entire system. Usually, the timing during this phase of the project has to be as short as possible. It is hopefully to avoid any failure, even for single subsystem components, during the tests that would compromise the validation and/or analysis of the entire system. Thus, the adoption of AM prototypes could be an interesting option to reduce the timing, but on the other hand it has to ensure the proper structural reliability in order to guarantee the fulfilment of the entire test and to evaluate all the related outputs. This specific issue was evaluated during the present paper. At this purpose, preliminary FEA were performed to confirm that the current configuration of the prototype was the most proper to the fulfilment of the test or if any changing (i.e. design) is needed.

First, to determine the forces acting on the rocker arm starting from the engine system input, the entire model was defined, and multibody analyses were performed using MSC/Adams. The model is composed of all engine elements connected to the rocker arm. This allowed for the calculation of the forces operating on the rocker arm. Fig. 1 shows the engine system model, where the rocker arm is composed of two different bodies (1, 2), and the valve bridge is composed of four different single valves (3), a valve spring (4), and an adjustment screw (5). Real engine conditions were imposed by setting the rotation of the camshaft (6) at 1200 revolutions per minute (rpm) and the load acting on the valve spring varied between 780 N and 1370 N. The model implemented in MSC/Adams calculates the forces acting on the adjustment screw, which are then used as inputs for the structural FEA of the rocker arm system performed in MSC/Apex. Each rotation of the camshaft generates a pulsed load cycle from zero to the maximum load on the adjustment screw (2.1 kN, see Fig. 4). In addition, a load of 100 kN was applied to the rocker shaft screw, based on field measurements. The general configuration of the components involved in the simulation is illustrated in Fig. 1. Some subcomponents of the system, in addition to those already mentioned in Fig. 1, are identified in Fig. 4 and named (6) camshaft, (7) roller, (8) rocker shaft, and (9) rocker shaft screw.

An elastic modulus of 212000 MPa and a Poisson coefficient of 0.29 were considered for rocker arm and rocker arm shaft. MSC/Apex was used to generate the mesh, which consisted of tetrahedral elements with quadratic features, adhering to the specified parameters: Jabobiano >0.7; Aspect Ratio < 5; Tetra Collapse > 0.15; Volume Skew < 0.95. The mesh consisted of roughly 350000 elements for rocker arm and rocker arm shaft. The cam body and the shaft were composed of about 36000 and 88000 elements.

A mesh-independent tie tool was adopted at the interface of the different bodies in contact with each other. A node-to-segment glued contact formulation was applied to account for the interactions between roller and camshaft. The contact tolerance was 1 mm.

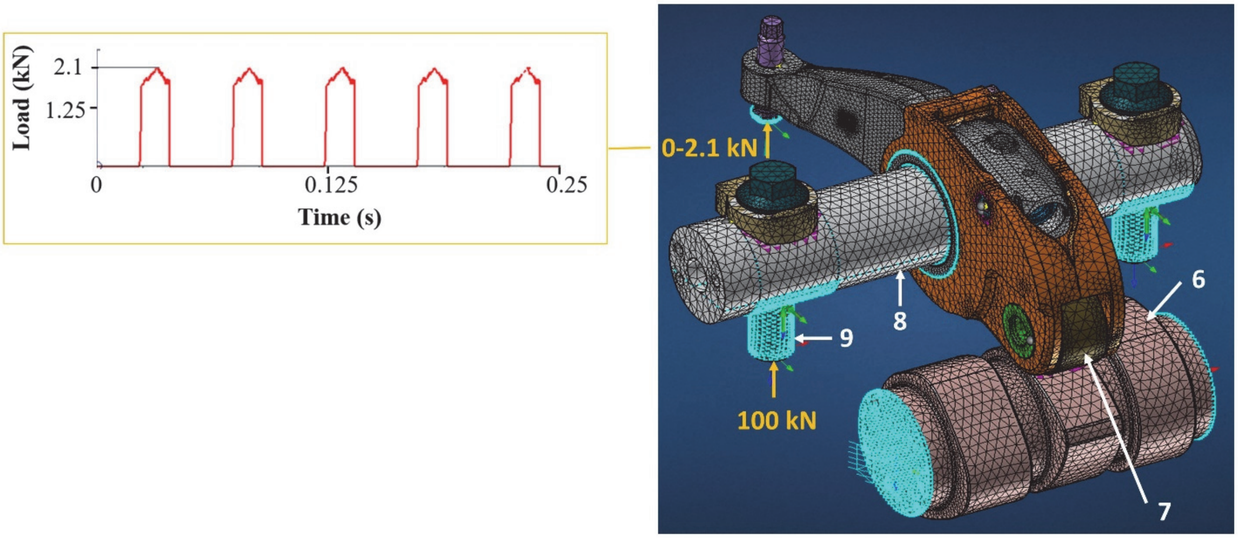

Figure 4: FEA model and loads applied at adjustment screw and rocker shaft screw.

The results were analyzed focusing on the behavior of the cam body (see element 1 in Fig. 1) to confirm that the design of this component could withstand real engine conditions. Based on these analyses, the rocker arms were prototyped using the LPBF technique in 17-4PH steel and tested on a functional engine test bench to characterize the assembly and validate the FEA simulation and component design.

Engine test bench

The prototypes were tested on a bench that was specifically developed and manufactured at the Streparava SpA testing center. The switchable rocker arms were assembled on a rocker arm shaft equipped with a camshaft and valves on a complete cylinder head. These elements constitute the entire system necessary for replicating the boundary conditions and constraints present on the engine, and for reproducing the loads generated by the shaft movements on the rocker arm. The assembly was driven by an electric asynchronous induction engine (Siemens series 1LE1 22Kw, 1500Rpm) directly connected to the camshaft and controlled by an inverter to simulate the actual engine speed, which was settled between 300-1200 Rpm. It should be noted that the maximum Rpm speed was the same as that analyzed during FEA. Signal acquisition cards were Siemens digital input SM 1221 and Siemens analog input SM 1231 4AI. The test was conducted under lubricated conditions, with oil pressure and temperature representative of real engine conditions, using synthetic SAE 0 W-20 oil. A photograph of the engine test bench during its operation at the Streparava testing center is shown in Fig. 5.
The test bench is a preliminary test crucial for validating the FEA simulation results, component design, and specific switchable rocker arm functionality. This study focuses on the behavior of the LPBF cam body after an operational test.

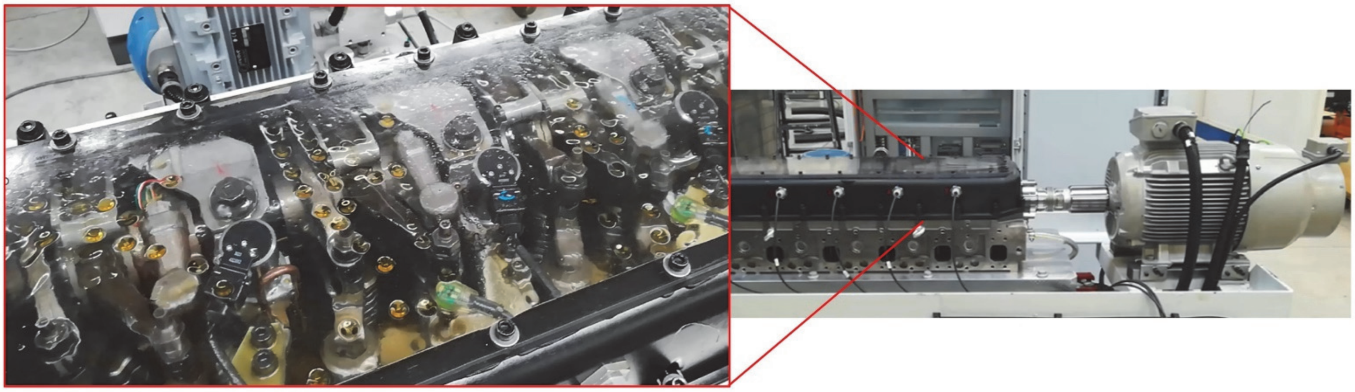

Figure 5: Engine test bench during its operation at Streparava testing centre.

RESULTS AND DISCUSSION

Microstructural analysis

Before starting with the analysis description, it would be useful to introduce some considerations regarding the general features of the as-built LPBF 17-4PH microstructure. For the alloy produced under these conditions, it is very difficult to discern between α-martensite and δ-ferrite using standard metallographic characterization methods. Indeed, the low carbon concentration of 17-4PH powder leads to a decrease in martensite tetragonality and its expansion along the C-axis, which is very similar to the crystal structure of δ-ferrite (body-centered cubic (BCC)) [35]. In the literature [36,37] it was demonstrated that the lattice parameters of α-martensite and δ-ferrite were very similar for $C < 0.07$ wt%.
Fig. 6 reports the optical microstructures at different magnifications of LPBF 17-4PH As-Built samples, both flat and cylindrical, along Transversal (T) and Longitudinal (L) sections. The first consideration is that the flat samples show a finer microstructure than the cylindrical ones in both the examined sections. An explanation can be found in the higher cooling rate during the process due to the lower sample thickness and minor cross-sectional area, which results in faster cooling. For cylindrical samples, larger grains oriented toward the build direction were observed. The thermal conditions of LPBF promote an epitaxial growth of columnar grains due to remelting of previously solidified material [38-40]. This can determine the microstructural anisotropy and a consequent embrittlement of the material. The arc-shaped melt pools (examples highlighted in red for the flat longitudinal sections in Fig. 6) are visible in both cylindrical and flat samples with preferred directional growth of the grains toward the center of the melt pool [16].
The solid-state phase transformation of 17-4PH is traditionally manufactured as follows: transformation of δ-ferrite into austenite and then into α-martensite [41] leading to a fully martensitic microstructure. These sequences cannot be the same for the LPBF technique, which is a non-equilibrium solidification process. Indeed, the cooling rates involved were high

(~10^6 K/s), and the columnar epitaxial grains removed the nucleation barrier and promoted the growth of the phase at the highest temperature. An aspect related to these cooling rates is the suppression of the transformation, resulting in a δ-ferrite microstructure, which is thermodynamically stable at low temperatures; thus, no other transformation is expected [36;42-43]. Other aspects contribute to the phase transformation sequence. Among these, the ratio of Chromium equivalents/Nikel equivalents (Cr_{eq}/Ni_{eq}) of the powder plays a crucial role in the solidification mechanism [44]. If this ratio is above 1.7-2, the growth rate of austenite is not sufficient for its nucleation from the liquid; therefore, the first solidified phase is δ-ferrite. The ratio for the present alloy, calculated using the equations reported in [45], is $Cr_{eq}/Ni_{eq} = 2.8$; therefore, δ-ferrite is expected to be formed. This is in agreement with the microstructures observed in other studies [37;45-48]. It is important to mention that some studies [12,14,16,44] claimed a mixture of martensite and retained austenite (i.e., austenite that does not transform to martensite upon cooling) for the as-built microstructure. Indeed, the cooling rates are high enough for martensite formation, but the refined austenitic grain size induced by this process can reduce the martensite start (M_s), leading to the presence of retained austenite owing to incomplete martensite transformation [44]. The presence of elements such as carbon, nitrogen, and nickel also promotes austenite stabilization. In addition, the austenite shape influences the transformation; block-shaped austenite is less stable and transforms more easily to martensite than acicular and lath-type austenite [49]. Finally, the gases used for powder atomization and/or the LPBF chamber atmosphere can affect the phase transformation [13,41]. Argon, which was used in the present work, seems to mainly induce the presence of a BCC structure (martensite or ferrite).

All these considerations allowed to conclude that the as-built LPBF 17-4PH samples show an anisotropic microstructure, likely composed mainly of δ-ferrite with a modest amount of martensitic needles and traces of equiassic retained austenitic grains at the melt pool boundary.

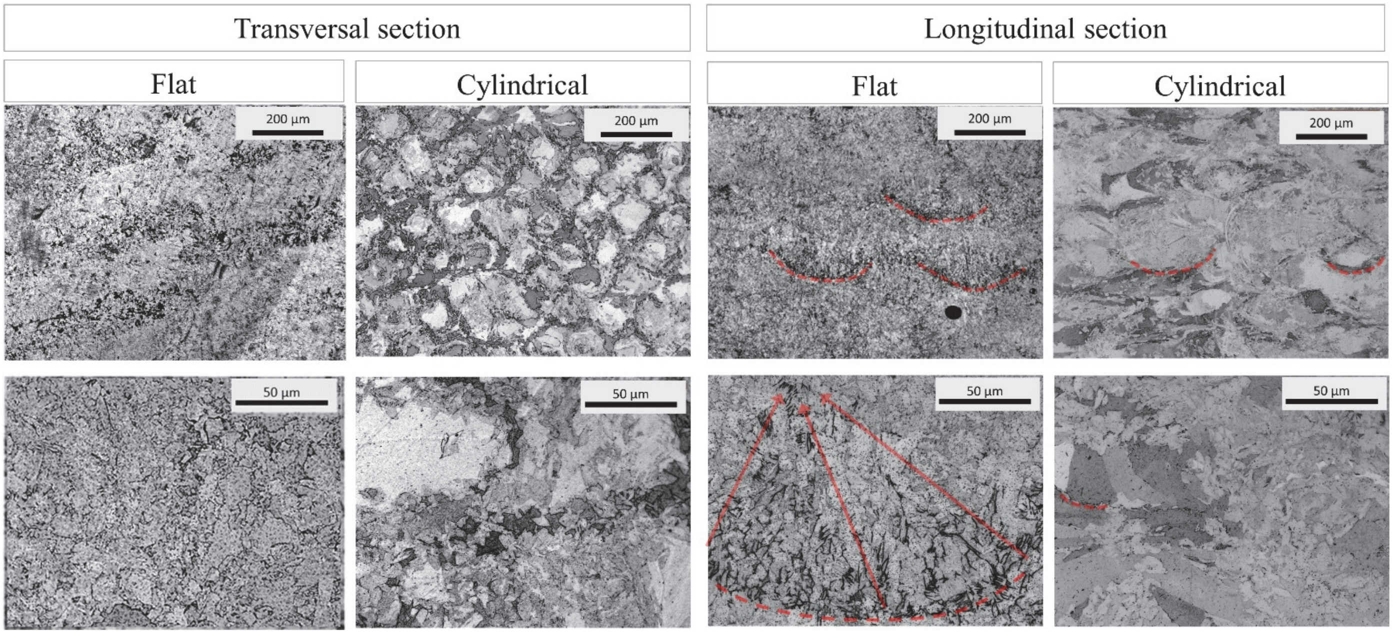

Figure 6: Optical microstructure of LPBF 17-4PH As-Built flat and cylindrical samples of transversal (T) and Longitudinal (L) sections at different magnifications.

In Fig. 7 the microstructures of LPBF 17-4PH at different magnifications after solution heat treatment are shown for both sample shapes (flat and cylindrical) and for one of the sections cut from the component. A very similar microstructure was observed for all the analyzed cases. The thermal treatment removed the typical features of the as-built state shown in Fig. 6 (interface regions of the deposited layers, melt pool boundaries, and grains elongated in the build direction), showing a homogeneous and isotropic aspect of the structure. In Fig. 7, martensitic laths are clearly visible in all microstructures reported, owing to the transformation from δ-ferrite to martensite after solubilization. Another consequence is a reduction in the volume fraction of the retained austenite after solubilization. Thermal treatment altered the stability of austenite and facilitated its transformation to martensite. The prior austenitic grain boundaries are not visible, probably because the starting microstructure consists of coarse ferrite grains, which can influence the nucleation and growth of austenite.

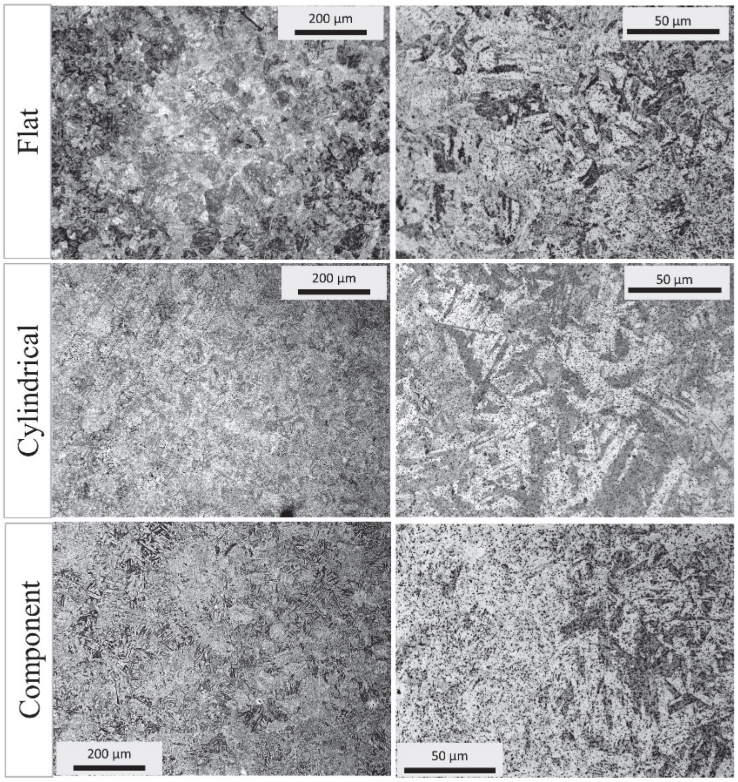

Figure 7: Optical microstructure of LPBF 17-4PH solutioned for both samples (flat and cylindrical) and component sections at different magnifications.

Fig. 8 reported SEM images on flat samples both in as-built and solutioned state. Similar considerations can be extended to cylindrical samples, as can be observed from the analyses reported in the supplementary material section (fig. 15).
SEM investigations confirmed that the as-built microstructure is expected to be composed of large columnar δ-ferrite grains, small island of martensite and retained austenite. After the solution treatment, it can be noted the presence of martensite with some islands of primary austenite. The grains size increased for all the constituents due to high temperature exposure that leads to recrystallization and faster grain growth. It can be noted from EDS analysis a difference of Cu content between martensite and the matrix after solubilization. In particular in elemental mapping analyses in Fig. 9 are visible a large number of ε-Cu precipitates particularly concentrated along the martensite lath. Also these analyses confirmed the previous comments gathered from OM.

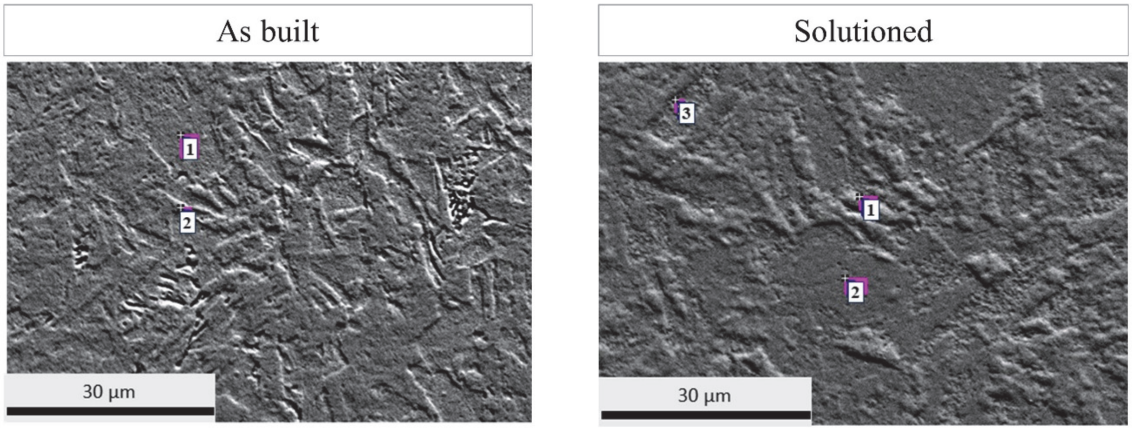

	Si	Cr	Fe	Ni	Cu
1	0.71	17.16	73.81	4.49	3.83
2	0.89	17.31	73.19	5.22	3.39

	Si	Cr	Fe	Ni	Cu
1	0.73	16.32	67.16	5.24	10.55
2	0.64	17.58	72.75	6.00	3.03
3	0.57	16.96	73.18	5.34	3.95

Figure 8: SEM images and EDS analysis of LPBF 17-4PH as built and solutioned for flat samples.

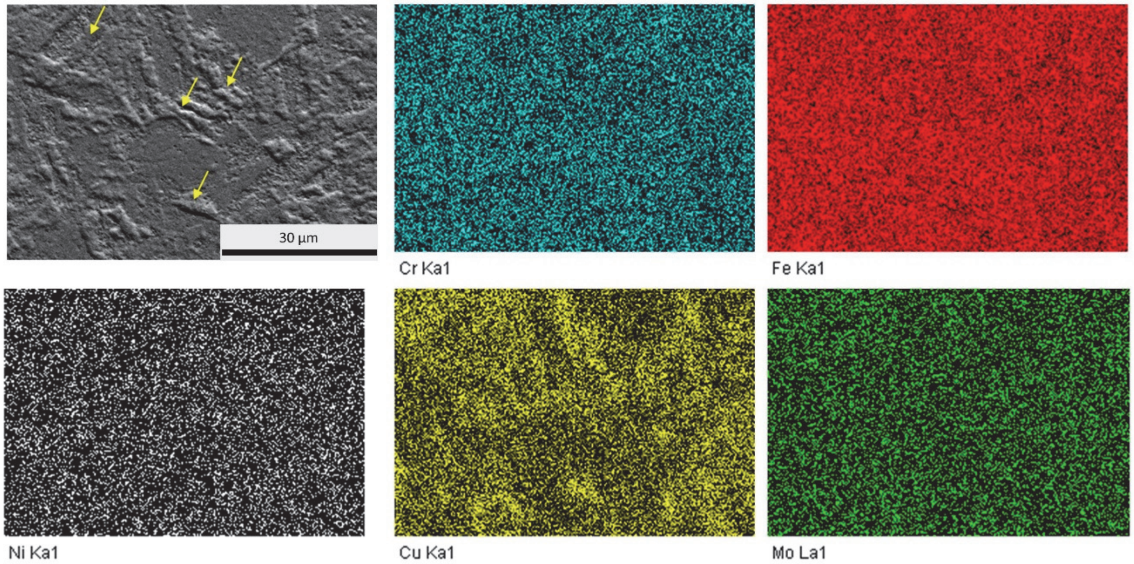

Figure 9: Elemental mapping analysis of LPBF 17-4PH solutioned for flat samples. Yellow arrows indicate the areas with higher Cu concentration.

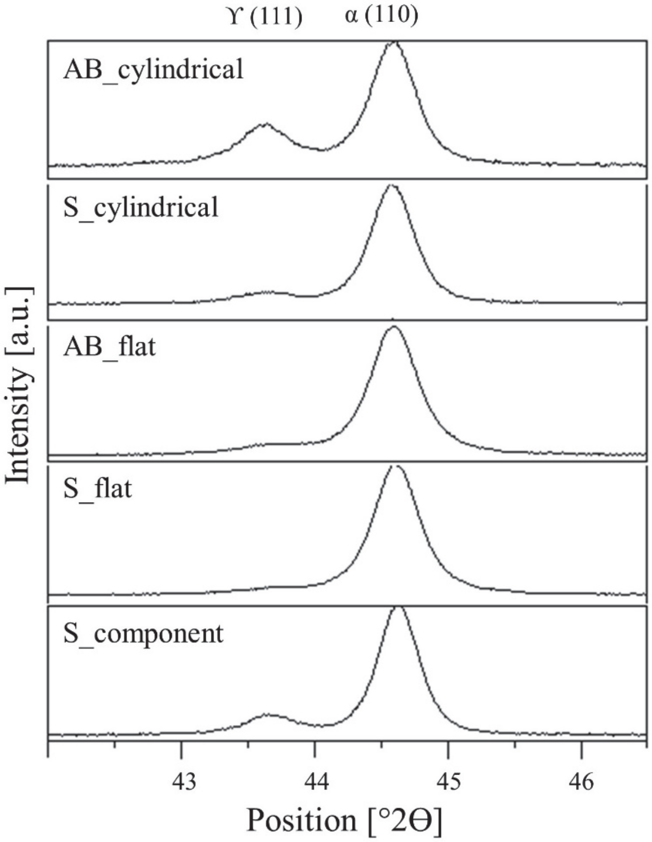

Figure 10: XRD data from the As-built (AB) and solutioned (S) 17-4 PH samples.

Fig. 10 shows the XRD patterns obtained from the analysis of transversal sections of the various conditions analyzed. The lattice distortion entity in the body-centered tetragonal (BCT) martensite for this alloy is very low, due to the limited C concentration (0.036 wt%). As a consequence, XRD technique cannot discerned between peaks corresponding to body-centered cubic (BCC) ferrite and BCT martensite, as also reported by Sun et al. [51] and by Alnajjar et al [52]. Therefore, in line with established practice for 17-4PH, both ferrite and martensite are considered to exhibit the BCC structure [51, 52], a convention adhered to in the current study. XRD phase analysis confirms the predominance of the BCC phase (α peak) with a minor presence of FCC phase (ϒ peak), indicating retained austenite. Comparing the same geometry of as-built (AB) and solutioned (S) samples (AB_cylindrical vs S_cylindrical and AB_flat vs S-flat) a reduction of ϒ peak after heat treatment is revealed. ϒ peaks intensity is more pronounced for samples having higher volume (component>cylindrical>flat), confirming the presence of a shape effect.

TENSILE PROPERTIES

Tab. 2 lists the average values and standard deviations of the mechanical properties of the flat and cylindrical specimens, both in the as-built and solution-heat-treated conditions. Fig. 11 shows the stress-deformation curve for each condition tested. One curve for each condition was selected to guarantee a readable format for comparison purposes. The highest yield strength was considered as a selection criterion among the curves of the same batch.

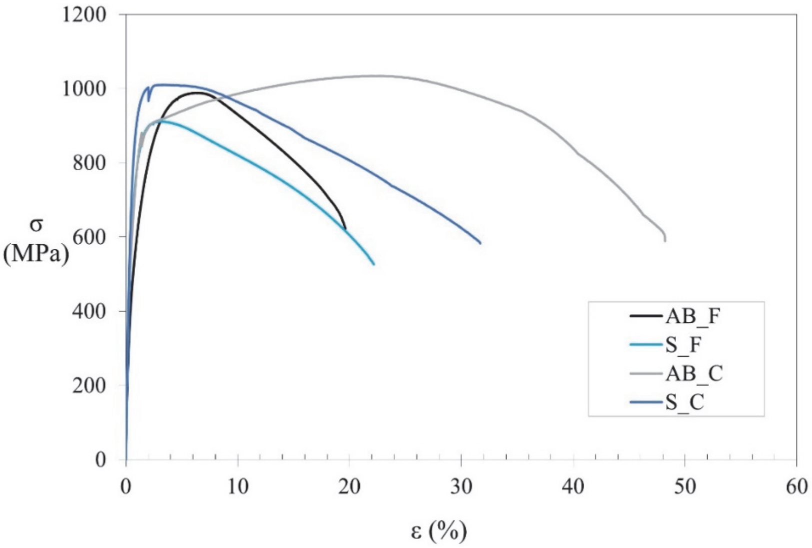

Figure 11: Stress-deformation curves for as-built (AB) and solutioned (S) samples, both in a flat (F) and cylindrical (C) configuration. At least three tests for each condition were performed.

	$\sigma_{p0.2}$ [MPa]	σ_m [MPa]	E [GPa]	A (%)
AB_Flat	472 ± 46	992 ± 6	151 ± 4	18 ± 6
AB_Cylindrical	576 ± 11	1030 ± 4	189 ± 18	48 ± 3
S_Flat	620 ± 24	917 ± 5	152 ± 12	20 ± 1
S_Cylindrical	768 ± 3	1008 ± 3	183 ± 4	31 ± 1

Table 2: Tensile properties for as-built (AB) and solutioned (S) samples, both in a flat (F) and cylindrical (C) configuration.

Regarding the shape factor effect, it is possible to note that, for the two conditions analyzed, all the mechanical properties decrease with sample volume (from cylindrical to flat samples; volumes of 2011 mm^3 and 270 mm^3 respectively). This trend is in accordance with the few works found in the literature on different steel Additively Manufactured (AMed) alloys [29-33] and suggests mainly the influence of the surface roughness. As is well-known, surface irregularities are a typical feature of this technology, and their impact on the mechanical properties becomes more significant as the surface-area-to-volume ratio increases, typically associated with lower thickness [29]. Additional details about these researches are summarized into the introduction section. The specimens analyzed during the present work had surface are/volume ratio 1.1 mm^{-1} and 0.5 mm^{-1} for flat and cylindrical samples respectively. Consequently, the reduction in tensile properties observed in flat samples compared to cylindrical ones under the same thermal treatment conditions can be attributed to the decrease in wall thickness in AM parts, consistently with the previously mentioned surface irregularities theory. In addition, other studies have reported that for small thicknesses, the mechanical properties deteriorate due to the reduced thickness-to-grain size [32,33]. It has been explained that the deformation was localized earlier when the amount of load-bearing material is reduced. The number of grains around the sample thickness modifies the deformation mechanism, potentially leading to a decrease in mechanical properties [50]. Additionally, in thinner samples, voids/defects are closer to the part surface, increasing the probability of failure occurring earlier in the plastic regime [29]. These additional explanations remain in accordance to the decrease of mechanical properties from cylindrical to flat samples observed in the current research. To better analyze this topic, in Fig. 12 the tensile properties are reported as a function of the surface area/volume (the ratio is 0.5 mm^{-1} and 1.1 mm^{-1} for cylindrical and flat samples respectively). It can be seen that the yield strength, ultimate tensile strength, elongation at failure, and elastic modulus decrease with decreasing sample size when considering equal heat treatment conditions (AB_cylindrical vs. AB_flat and S_cylindrical vs. S_flat). Looking at the standard deviations (both in Fig. 12 and Tab. 2), it can be noted that the variability of the yield strength increased as the sample size decreased, as also observed by Chan et al. [33]. However, the widespread elongation to failure observed in some samples is typical for AM materials. In addition, elevated amounts of Ni and Cr can induce the formation of metastable retained austenite in the matrix, which can be transformed to martensite by plastic deformation during the tensile test (TRansformation Induced by the Plasticity (TRIP) effect), causing significant work-hardening and increased ductility [36].

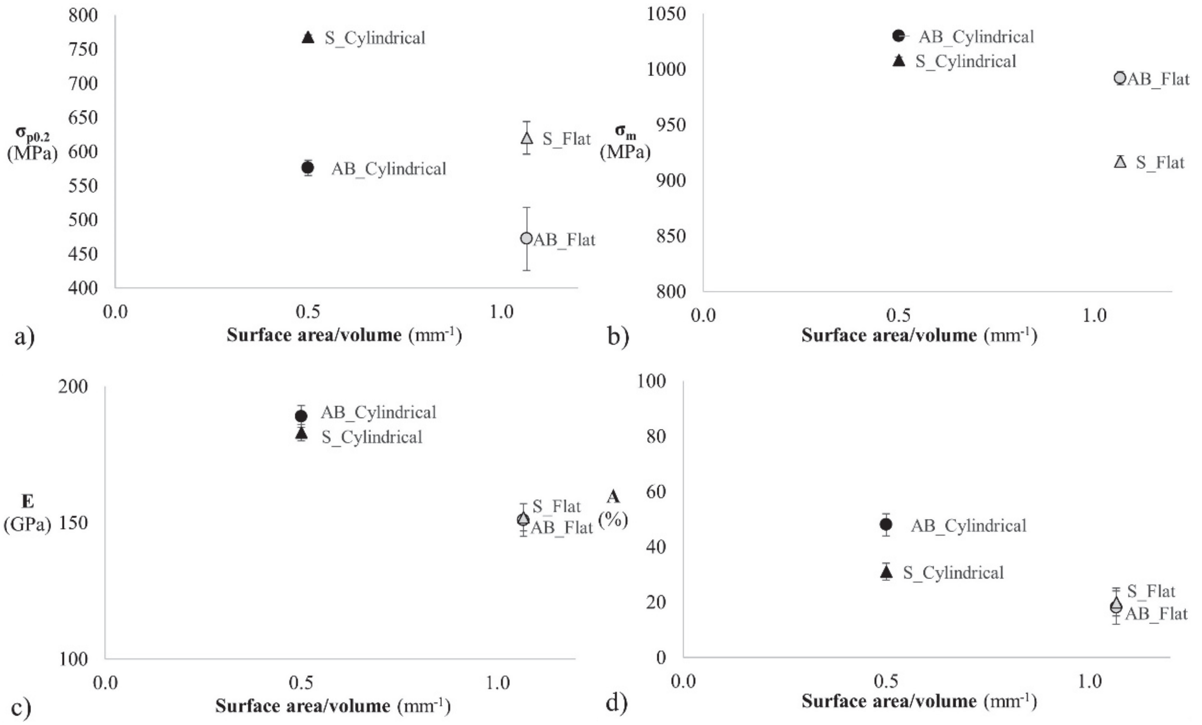

Figure 12: Tensile properties as a function of the sample size: a) yield strength; b) ultimate tensile strength; c) elastic modulus; d) elongation at failure.

The analysis of the shape effect on the mechanical properties for these particular samples highlighted that there is a dependence between the tensile properties and LPBF component thickness, and it can be concluded that when designing AM parts, it is essential to consider that the resistance of thin sections can be different from that expected from bulk material properties.

The effect of heat treatment on the mechanical properties was similar for the cylindrical and flat samples. Indeed, solubilization led to an increase in the yield strength of 31% and 33%, a slight decrease in ultimate stress of -8% and -2%, and a variation in elongation percentages of +11% and -35% (percentages referred to as flat and cylindrical samples, respectively). This influence on the mechanical strength can be ascribed to the transformation of δ-ferrite in martensite [14,53] and can confirm the reduction in the retained austenite volume fraction after heat treatment, as described in the microstructural analysis section. The major isotropy and homogeneity of the microstructure can also affect the increase in the strength. The reduction in elongation in the solubilized cylindrical samples can again be related to the presence of martensite, while the unexpected almost null variation of this parameter for flat samples (clearly visible in Fig. 7 d) has to be attributed to the high variability of this parameter for AM products.

HARDNESS TEST

Vickers microhardness profiles were obtained for the transverse and longitudinal sections of the samples (flat and cylindrical) and components, as shown in Fig. 13. Tab. 3 reports the average HV values and their standard deviations for the different configurations analyzed. First, it can be noted that cylindrical samples have the highest hardness values, particularly in the longitudinal section. This confirmed the shape effect explained in the tensile test section. However, the transverse sections showed similar values without any evident dependence on the thickness when the heat treatment conditions were comparable. The different trends between the transverse and longitudinal sections highlight the anisotropic behavior of the LPBF samples. The shape effect is confirmed again by the similar average values found between the component and flat sample shapes, having analogous thickness values (4.5 and 3 mm, respectively).

The as-built condition had a slightly higher hardness than the solubilized condition for both flat and cylindrical specimens. This could be linked to the presence of higher residual stresses under the AB conditions. The high cooling rate generated by the process is associated with high residual stresses, both because of the high solidification rate and the presence of solutes in the matrix, which cause lattice distortion [37]. Finally, from Fig. 13 it can be observed that some fluctuations were registered along the profile, probably owing to the different microstructures found in the correspondence of the specific and local microhardness indentations.

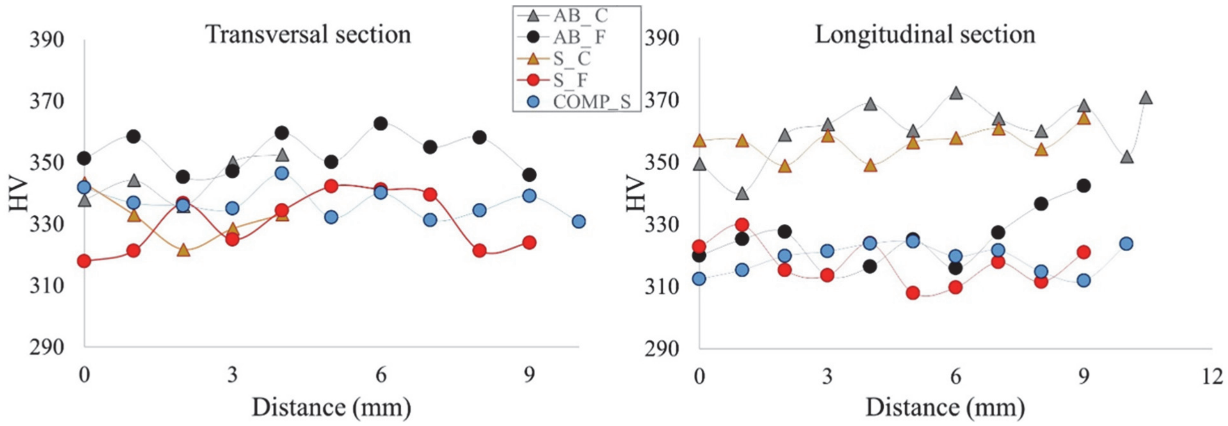

Figure 13: Microhardness profile of transversal (left) and longitudinal (right) sections for As-Built (AB) and Solutioned (S) samples having Cylindrical (C) and Flat (F) shape and for the component in the solubilized state (Comp_S).

	Flat samples (th=3mm)		Component (avg th=4.5 mm)		Cylindrical samples (th= 8 mm)	
	L	T	L	T	L	T
AB	325 ± 9	353 ± 6	/	/	361 ± 10	347 ± 8
S	317 ± 7	330 ± 9	319 ± 5	337 ± 5	356 ± 5	330 ± 7

Table 3: Vicker's microhardness of the different samples in the as-built (AB) and solution (S) heat treatment (HT) conditions. Longitudinal (L) and Transversal (T) sections were analyzed. An indication of the average thickness (th) of the samples is reported for a better comprehension of the results.

RESULTS FROM FEA

The output of the multibody MSC/Adams simulations was the force acting on the adjustment screw, which resulted in a pulsed load cycle from zero to the maximum load on the adjustment screw (2.1 kN, see Fig. 4). The results of the FEA of MSC/Apex are shown in Fig. 14. Here, the blue areas correspond to low stress, whereas the red and yellow areas indicate increasing solicitations. It can be noted that the mechanical stresses acting on the component are generally very low (maximum value of the threshold, 20 MPa). The overall stresses are well below the yield strength of the alloy, and the fulfilment of the resistance limits for the cam body preliminarily confirms its mechanical resistance during the test owing to the proper selection of the material and design.

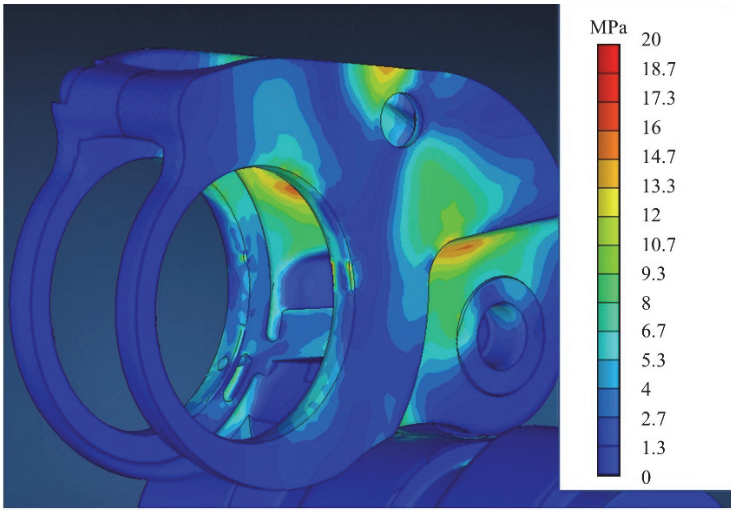

Figure 14: MSC/Apex Von Mises output about Stress distributions on the rocker arm.

ENGINE TEST BENCH RESULTS

The engine test bench was completed without any structural failure, which validated the adoption of a 17-4PH alloy LPBFed prototype. The employment of LPBF allowed the respect of the strict project timing, without any implication on the overall testing activity that had wider purposes. Indeed, the proper functioning of the entire system was checked during the present test and the relevant information gathered from the specific LPBFed subcomponent under investigation is its structural resistance till the end of the experimental activity.

The main result was that the project aim was achieved, which allowed for a time-effective structural test to verify the functionality of the innovative system.

CONCLUSIONS

The objective of this study was to evaluate the reliability of AM applications for the structural prototype of a new powertrain system, a rocker arm, finalized to reduce vehicle emissions. Samples and real prototypes were studied, and the impacts of sample geometry and size, as well as the effects of heat treatment, were analyzed.

The following conclusions can be retrieved:

- Microstructure: smaller samples (flat shape) have a finer microstructure than larger ones (cylindrical), probably because of the higher cooling rate related to the lower thickness. The as-built microstructure was anisotropic and composed mainly of δ-ferrite with a small number of martensitic needles and equiassically retained austenitic grains at the melt pool boundary (as deduced from experiments and the literature). After the solution treatment, a homogeneous and isotropic macrostructure was observed, and δ-ferrite was transformed into martensite.
- Tensile: all mechanical properties decreased when the surface area/volume (SA/V) increased. This trend suggests the influence of both surface irregularities, typical of this technology, having an increasing effect for lower SA/V and thickness/grain size reduction, which induces earlier localization of deformation. The effect of heat treatment on the mechanical properties of the cylindrical and flat samples was similar, and after solubilization, the yield strength increased and the ultimate stress slightly decreased (average variation $\sigma_{p0.2}$= 32% and σ_m=-5%). This influence on the mechanical strength can be ascribed to the transformation of δ-ferrite in martensite and confirms the reduction in the retained austenite volume fraction after heat treatment.
- Hardness: the shape effect was confirmed (the cylindrical samples had the highest hardness values). The as-built condition had a slightly higher hardness than the solubilized condition on both the flat and cylindrical specimens, which could be linked to the presence of higher residual stresses in the AB condition.
- Finite element analysis: the overall stresses are well below the yield strength of the alloy, and the fulfillment of the resistance limits for the cam body preliminarily confirms its mechanical resistance, achieved thanks to the proper selection of material and design.

- Engine test bench: the test bench was successfully completed without any structural failure, which validates the adoption of a 17-4PH alloy LPBFed prototype.

In conclusion, the feasibility of an additive manufacturing application for this particular structural prototype was demonstrated. In this context, it was seen that it is fundamental a conscious selection of the material and heat treatment in relation to the component design, considering the specific features of LPBFed alloys. The conclusions of this project set the basis for similar future applications of time-effective prototypes that can be dimensioned owing to appositely developed postprocesses that guarantee the required resistance.

SUPPLEMENTARY MATERIAL

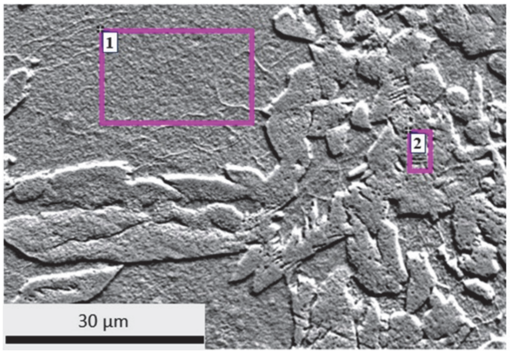

	Si	Cr	Fe	Ni	Cu
1	0.52	16.96	74.20	4.35	3.97
2	0.58	17.43	73.68	4.17	4.14

Figure 15: SEM images and EDS analysis of LPBF 17-4PH as built for cylindrical samples.

ACKNOWLEDGMENTS

The authors are grateful to: the staff members of the Streparava Testing Center, particularly to Ing. Luca Cordioli and Ing. Fabio Cibolini for their support in conducting fatigue bench tests; to Dr Annalisa Zacco and Chem4Tech laboratory for the XRD measurements.

FUNDING STATEMENT

The funders had no role in the study design, data collection and analysis, decision to publish, or manuscript preparation.

ETHICAL COMPLIANCE

All procedures performed in this study involving human participants were in accordance with the ethical standards of the institutional and/or national research committee and with the 1964 Helsinki Declaration and its later amendments or comparable ethical standards.

REFERENCES

[1] Satish Prakash, K., Nancharaih, T., Subba Rao ,V.V. (2018). Additive Manufacturing Techniques in Manufacturing -An Overview, Mater. Today: Proc., 5 (2-1), pp. 3873-3882, DOI: 10.1016/j.matpr.2017.11.642.

[2] Cecchel, S., Ferrario, D., Cornacchia, G., Gelfi, M. (2020). Development of heat treatments for Selective Laser Melting Ti6Al4V alloy: effect on microstructure, mechanical properties, and corrosion resistance, Advanced Engineering Materials, 22(8), pp. 2000359, DOI: 10.1002/adem.202000359.

[3] Cecchel, S., Ferrario, D., Mega, F., Cornacchia, G. (2022). Wear and Corrosion Characterization of a Ti–6Al–4V Component for Automotive Applications: Forging versus Selective Laser Melting Technologies, Advanced Engineering Materials, 24(8), pp. 2200082, DOI: 10.1002/adem.202200082.

[4] Cecchel, S., Ferrario, D., Mega, F., Cornacchia, G. (2021). Numerical, Mechanical, and Metallurgical Investigation of an Innovative Near Net Shape Titanium Selective Laser Melting Engine Component and Comparison with the Conventional Forged One, Advanced Engineering Materials, 23(7), pp. 202100036, DOI: 10.1002/adem.202100036.

[5] Automotive 3D printing applications. Available at: https://www.hubs.com/knowledge-base/automotive-3d-printing-applications/, [accessed 22/11/2023].

[6] Elverum, C. W., Welo, T. (2014). The Role of Early Prototypes in Concept Development: Insights from the Automotive Industry, Procedia CIRP, 21, pp. 491-496, DOI: 10.1016/j.procir.2014.03.127.

[7] Husain, S. M., Sheikh, S. (2013) Design and analysis of a rocker arm, Int. J. Mech. Eng. & Rob. Res., 2(3), pp. 191-197, available at https://www.ijmerr.com/uploadfile/2015/0409/20150409050614852.pdf

[8] Ferrario, D., Mega, F., Magni. M. (2022). switchable rocker arm for controlling the lift of a valve bridge or a single valve of valve train group of an internal combustion engine and valve train group comprising at least a such switchable rocker arm, PCT patent number WO2022/069998 A1.

[9] Lin, X., Cao, Y., Wu, X., Yang, H., Chen, J., Huang, W. (2012). Microstructure and mechanical properties of laser forming repaired 17-4PH stainless steel, Mater. Sci. Eng. A, 553, pp. 80-88, DOI: 10.1016/j.msea.2012.05.095.

[10] Rashid, R., Masood, S.H., Ruan, D., Palanisamy, S., Rahman Rashid, R.A., Brandt, M. (2017). Effect of scan strategy on density and metallurgical properties of 17-4PH parts printed by Selective Laser Melting (SLM), J. Mater. Process. Technol., 249, pp. 502-511, DOI: 10.1016/j.jmatprotec.2017.06.023.

[11] Mahmoudi, M., Elwany, A., Yadollahi, A., Thompson, S.M., Bian, L., Shamsaei, N. (2017). Mechanical properties and microstructural characterization of selective laser melted 17-4 PH stainless steel. Rapid Prototyp. J., 23(2), pp. 280-294, DOI: 10.1108/RPJ-12-2015-0192.

[12] Facchini, L., Vicente, N., Lonardelli, I., Magalini, E., Robotti, P., Alberto, M. (2010). Metastable Austenite in 17–4 Precipitation-Hardening Stainless Steel Produced by Selective Laser Melting, Adv. Eng. Mater., 12(3), pp. 200900259, DOI: 10.1002/adem.200900259.

[13] Murr, L.E., Martinez, E., Hernandez, J., Collins, S., Amato, K.N., Gaytan, S.M., Shindo, P.W. (2012). J. Microstructures and Properties of 17-4 PH Stainless Steel Fabricated by Selective Laser Melting, J. Mater. Res. Technol., 1(3), pp. 167-177, DOI: 10.1016/S2238-7854(12)70029-7.

[14] LeBrun, T., Nakamoto, T., Horikawa, K., Kobayashi, H. (2015). Effect of retained austenite on subsequent thermal processing and resultant mechanical properties of selective laser melted 17–4 PH stainless steel, Mater. Des., 81, pp. 44-53, DOI: 10.1016/j.matdes.2015.05.026.

[15] Cheruvathur, S., Lass, E.A., Campbell, C.E. (2016). Additive Manufacturing of 17-4 PH Stainless Steel: Post-processing Heat Treatment to Achieve Uniform Reproducible Microstructure, Jom. 68, pp. 930–942, DOI: 10.1007/s11837-015-1754-4.

[16] Yadollahi, A., Shamsaei, N., Thompson, S.M., Elwany, A., Bian, L. (2015). Mechanical and Microstructural Properties of Selective Laser Melted 17-4 PH Stainless Steel, ASME Int. Mech. Eng. Congr. Expo. Proc., pp. 1-7, DOI: 10.1115/IMECE2015-52362.

[17] Rafi, H.K., Pal, D., Patil, N., Starr, T.L., Stucker, B.E. (2014). Microstructure and Mechanical Behavior of 17-4 Precipitation Hardenable Steel Processed by Selective Laser Melting, J. Mater. Eng. Perform., 23, pp. 4421–4428, DOI: 10.1007/s11665-014-1226-y.

[18] Starr, T.L., Rafi, H.K., Stucker, B.E., Scherzer, C.M. (2012). Controlling phase composition in selective laser melted stainless steels, available at: https://utw10945.utweb.utexas.edu/Manuscripts/2012/2012-33-Starr.pdf (accessed 04/12/02023).

[19] Pasebani, S., Ghayoor, M., Badwe, S., Irrinki, H., Atre, S. V. (2018). Effects of atomizing media and post processing on mechanical properties of 17-4 PH stainless steel manufactured via selective laser melting, Addit. Manuf., 22, pp. 127-137, DOI: 10.1016/j.addma.2018.05.011.

[20] AlMangour, B., Yang, J.M. (2017). Understanding the deformation behavior of 17-4 precipitate hardenable stainless steel produced by direct metal laser sintering using micropillar compression and TEM, Int. J. Adv. Manuf. Technol., 90, pp. 119–126, DOI: 10.1007/s00170-016-9367-9.

[21] AlMangour, B., Yang, J.M. (2016). Improving the surface quality and mechanical properties by shot-peening of 17-4 stainless steel fabricated by additive manufacturing, Mater. Des., 110, pp. 914-924, DOI: 10.1016/j.matdes.2016.08.037.

[22] Bayode, A., Akinlabi, E.T., Pityana, S., (2016). Lect. Microstructure and Microhardness of 17-4 PH Stainless Steel Made by Laser Metal Deposition, WCECS 2016, San Francisco, USA,
available at: https://www.iaeng.org/publication/WCECS2016/WCECS2016_pp812-814.pdf

[23] Irrinki, H., Jangam, J.S.D., Pasebani, S., Badwe, S., Stitzel, J., Kate, K., Gulsoy, O., Atre, S. V. (2018). Effects of particle characteristics on the microstructure and mechanical properties of 17-4 PH stainless steel fabricated by laser-powder bed fusion Powder Technol., 331, pp. 192-203, DOI: 10.1016/j.powtec.2018.03.025.

[24] Tillmann, W., Dias, N. F. L., Stangier, D., Schaak, C., Höges, S. (2022). Heat treatment of binder jet printed 17–4 PH stainless steel for subsequent deposition of tribo-functional diamond-like carbon coatings, Mater. Des., 213, pp. 110304, DOI: 10.1016/j.matdes.2021.110304.

[25] Barba, D., Alabort, C., Tang, Y.T., Viscasillas, M.J., Reed, R.C., Alabort, E. (2020). On the size and orientation effect in additive manufactured Ti-6Al-4V, Mater. Des., 186, pp. 108235, DOI: 10.1016/j.matdes.2019.108235.

[26] Jia, G. (2017). The Effect of Oxygen Content on the Tensile Properties of SLMed Ti6Al4V Alloy, Thesis, Monash University, DOI: 10.4225/03/589ab048d408b.

[27] Yu, Q., Qi, L., Tsuru, T., Traylor, R., Rugg, D., Morris, J., Asta, M., Chrzan, D., Minor, A.M. (2015). Origin of dramatic oxygen solute strengthening effect in titanium, Science, 347, pp. 635-639, DOI: 10.1126/science.1260485.

[28] Kahveci, A., Welsch, G. (1986) Effect of oxygen on the hardness and alpha/beta phase ratio of Ti-6A1-4V alloy, Scr. Metall, 20, pp. 1287-1290, DOI: 10.1016/0036-9748(86)90050-5

[29] Leicht, A., Pauzon, C., Rashidi, M., Klement, U., Nyborg, L., Hryha, E. (2021). Effect of part thickness on the microstructure and tensile properties of 316L parts produced by laser powder bed fusion, Adv. Ind. Manuf. Eng., 2, pp. 100037, DOI: 10.1016/j.aime.2021.100037.

[30] Brown, B., Everhart, W., Dinardo, J. (2016). Characterization of bulk to thin wall mechanical response transition in powder bed AM, Rapid Prototyping J., 22(5), pp. 801-809, DOI: 10.1108/RPJ-10-2015-0146.

[31] Roach, A. M., White, B. C., Garland, A., Jared, B. H., Carroll, J. D., Boyce, B. L. (2020). Size-dependent stochastic tensile properties in additively manufactured 316L stainless steel, Additive Manufacturing, 32, pp. 101090,
DOI: 10.1016/j.addma.2020.101090.

[32] Kohyama A., Hamada K., Matsui H. (1991). Specimen size effects on tensile properties of neutron-irradiated steels. J. Nucl. Mater., 179-181 (1), pp. 417-420, DOI: 10.1016/0022-3115(91)90113-L.

[33] Chan, W.L., Fu, M.W. (2011). Experimental studies and numerical modeling of the specimen and grain size effects on the flow stress of sheet metal in microforming. Mater. Sci. Eng., 528 (25-26), pp. 7674-7683,
DOI: 10.1016/j.msea.2011.06.076.

[34] Matweb, material property data, 42CrMo4-3 6107 (M) Steel +QT. Available at: https://matweb.com/search/datasheet.aspx?matguid=6267555d6f8d4054bd841b7b512540fe&ckck=1, accessed 04/12/2023.

[35] Lashgari, H.R., Kong, C., Adabifiroozjaei, E., Li, S. (2020). Microstructure, post thermal treatment response, and tribological properties of 3D printed 17-4 PH stainless steel, Wear, 456-457, pp. 203367,
DOI: 10.1016/j.wear.2020.203367.

[36] Eskandari, H., Lashgari, H.R., Ye, L., Eizadjou, M., Wang, H. (2022). Microstructural characterization and mechanical properties of additively manufactured 17–4PH stainless steel, Materials Today Communications, 30, pp. 103075,
DOI: 10.1016/j.mtcomm.2021.103075.

[37] Meredith, S.D., Zuback, J.S., Keist, J.S., Palmer, T.A. (2018). Impact of composition on the heat treatment response of additively manufactured 17–4 PH grade stainless steel, Mater. Sci. Eng. A, 738, pp. 44-56,
DOI: 10.1016/j.msea.2018.09.066.

[38] Sun, Y., Hebert, R.J., Aindow, M. (2018). Effect of heat treatments on microstructural evolution of additively manufactured and wrought 17-4PH stainless steel, Mater. Des., 156, pp. 429-440, DOI: 10.1016/j.matdes.2018.07.015.

[39] Hui Xiao, M.C., Song, L. (2021). Direct fabrication of single-crystal-like structure using quasi-continuous-wave laser additive manufacturing, J. Mater. Sci. Technol., 60, pp. 216–222, DOI: 10.1016/j.jmst.2020.04.043.

[40] Basak, A., Das, S. (2016). Epitaxy and Microstructure Evolution in Metal Additive Manufacturing, Annu. Rev. Mater. Res., 46, pp. 125-149, DOI: 10.1146/annurev-matsci-070115-031728.

[41] Zai, L., Zhang, C., Wang Y., Guo, W., Wellmann, D., Tong, X., Tian, Y. (2020). Laser Powder Bed Fusion of Precipitation-Hardened Martensitic Stainless Steels: A Review, Metals, 10(2), pp. 255, DOI: 10.3390/met10020255.

[42] Alnajjar, M. (2019) Corrosion properties of 17-4 PH martensitic stainless steel obtained by additive manufacturing, [P.hD thesis], Lion (FR): University of Lyon.

[43] David, S.A., Vitek, J.M. (1989). Correlation between solidification parameters and weld microstructures, Int. Mater. Rev., 34(1), pp. 213-245, DOI: 10.1179/imr.1989.34.1.213.

[44] Yadollahi, A., Shamsaei, N., Thompson, S. M., Elwany, A., Bian L. (2017). Effects of building orientation and heat treatment on fatigue behavior of selective laser melted 17-4 PH stainless steel, Int. J. Fatigue, 94(2), pp. 218-235, DOI: 10.1016/j.ijfatigue.2016.03.014.

[45] Sabooni, S., Chabok, A., Feng, S. C., Blaauw, H., Pijper T. C., Yang H. J., Pei Y. T. (2021). Laser powder bed fusion of 17–4 PH stainless steel: A comparative study on the effect of heat treatment on the microstructure evolution and mechanical properties, Addit. Manuf., 46, pp. 102176, DOI: 10.1016/j.addma.2021.102176.

[46] Shirdel, M., Mirzadeh, H., Parsa, M. H. (2015). Nano/Ultrafine Grained Austenitic Stainless Steel through the Formation and Reversion of Deformation-Induced Martensite: Mechanisms, Microstructure, Mechanical Properties, and TRIP Effect, Mater. Charact., 46, pp. 102176, DOI: 10.1016/j.matchar.2015.03.031.

[47] Kotecki D., Lippold J., Hoboken N.J.B.B., Ureta E. (2011). Welding Metallurgy and Weldability of Stainless Steels, Hoboken, New Jersey, John Wiley & Sons, Inc., pp. 188–206, DOI: 10.1002/9781118960332.

[48] Suutala, N. (1983). Effect of solidification conditions on the solidification mode in austenitic stainless steels, Metall. Trans. A, 14, pp. 191–197, DOI: 10.1007/BF02651615.

[49] Choi, J.P., Shin, G.H., Yang, S., Yang, D.Y., Lee, J.S., Brochu, M., Yu, J.H. (2017). Densification and microstructural investigation of Inconel 718 parts fabricated by selective laser melting, Powder Technol., 310, pp. 60-66, DOI: 10.1016/j.powtec.2017.01.030.

[50] Strnadel, B., Brumek, J. (2013). Effect of tensile test specimen size on ductility of R7T steel. Proceedings of Metals 2013, 22nd International Conference on Metallurgy and Materials, Brno, Czech Republic, EU, pp. 560-565.

[51] Sun, Y., Hebert, R. J., Aindow, M. (2018). Effect of heat treatments on microstructural evolution of additively manufactured and wrought 17-4PH stainless steel, Materials and Design, 156, pp. 429–440, DOI: 10.1016/j.matdes.2018.07.015.

[52] Alnajjar, M., Christien, F., Wolski, K., Bosch, C. (2019). Evidence of austenite by-passing in a stainless steel obtained from laser melting additive manufacturing, Additive Manufacturing, 25, p. 187–119, DOI: 10.1016/j.addma.2018.11.004.

[53] Hsu, T. H., Chang, Y. J., Huang, C. Y., Yen, H. W., Chen, C. P, Jen, K. K., Yeh, A. C. (2019). Microstructure and property of a selective laser melting process induced oxide dispersion strengthened 17-4 PH stainless steel, J. Alloy Compd., 803, pp. 30-41, DOI: 10.1016/j.jallcom.2019.06.289.